Distribution of carbon in martensite during quenching and tempering of dual phase steels and consequences for damage properties

Irina Pushkareva, Philip Scott Colin, Mohamed Gouné, Nathalie Valle, Abdelkrim Redjaïmia, Antoine Moulin

ISIJ International, Vol. 53 (2013), No. 7, pp. 1215–1223

Distribution of Carbon in Martensite During Quenching and Tempering of Dual Phase Steels and Consequences for Damage Properties

Irina PUSHKAREVA,[1)]* Colin Philip SCOTT,[2)] Mohamed GOUNÉ,[3)] Nathalie VALLE,[4)] Abdelkrim REDJAÏMIA[1)] and Antoine MOULIN[2)]

1) Université de Lorraine, Institut Jean Lamour – CRNS – UMR 7198, Ecole des Mines de Nancy, Parc de Saurupt, F-54042 Nancy, France. 2) Arcelor Research SA, Voie Romaine – BP 30320, F-57283 Maizières-lès-Metz, France. 3) ICMCB-CNRS, 87 avenue du Docteur Schweitzer, 33609 Pessac, France. 4) Centre de Recherche Public Gabriel Lippmann, 41 rue du Brill, L-4422 Belvaux, Luxemburg.

(*Received on January 9, 2013; accepted on April 15, 2013*)

The microstructural evolution of martensite in as-quenched and quenched and tempered Fe–0.15C–0.215Si–1.9Mn–0.195Cr wt.% dual phase (DP) steels processed to give four different ferrite/martensite ratios was studied. It was found that partial thermodynamic equilibrium was obtained after intercritical annealing for 130 s. The local carbon distribution in as-quenched martensite was heterogeneous for all quenching temperatures. Significant carbon enrichment was observed at the ferrite/martensite interface at annealing temperatures of 790°C, whereas carbon depletion occurred when the annealing temperature was reduced to 755°C. A possible explanation for the carbon profile in terms of the effect of Mn partitioning on the austenite phase transformation kinetics is given. The kinetics of carbide formation during tempering is strongly influenced by these carbon gradients. A simple analysis shows that the interface carbon depletion observed at lower intercritical annealing temperatures could induce a beneficial increase in the void nucleation strain ε_n, due to a reduction in the backstress at the ferrite/martensite interface which decreases the local stress triaxiality. We estimate that the upper limit for the improvement in the as-quenched microstructure is ~8%, so the effect could provide a moderate delay in the onset of damage. Further, we propose that the improvement in damage resistance during tempering is mainly due to dispersed void formation at tempered carbides and that this mechanism will be compromised if those carbides are localised at ferrite/martensite interfaces. This argument mitigates for the carbon-depleted interface structure obtained at lower intercritical temperatures.

KEY WORDS: dual-phase; steel; microstructure; carbon distribution; phase transformation; thermodynamics; damage.

1. Introduction

Ferrite-martensite dual phase (DP) steels possess high strength, good formability and weldability and are rather straightforward to process.[1)] They are thus important materials for current weight reduction programs for automotive structural and safety related components.[2)] Current products with ~20% volume fraction martensite exhibit tensile strength levels in the 600 – 800 MPa range. Spot-weldability concerns mean that it is undesirable to increase DP carbon contents beyond ~0.15%, so that accessing higher strength grades (>1 000 MPa) requires either a strong reduction in the ferrite grain size or an increase in the martensite fraction.[3)] The first solution is generally not compatible with existing production tools, so commercial DP1000 grades are often quenched from higher intercritical temperatures and contain more martensite (30–50% vol.). However, the balance between martensite volume fraction and carbon content has a strong effect on important in-use properties such as stretch-flange formability and susceptibility to damage.[4)] These properties can be further modified in a quite complex manner by post-quench tempering, so that obtaining a final optimized product requires a detailed knowledge of the microstructure-properties relationships. The effects of microstructure variations on the ductility and damage behaviour of DP steels have been studied in detail by a number of authors using scanning electron microscopy (SEM),[4–7)] X-ray micro-tomography[8–10)] and digital image correlation (DIC)[11)] techniques. These studies have highlighted the importance of the volume fraction, morphology and carbon content of the martensite phase. Structure-properties models based on the strain hardening characteristics of ferrite and martensite have been proposed[12–14)] and extended to include the effects of statistically stored and geometrically necessary dislocations.[3)] Further, finite element based failure models

* Corresponding author: E-mail: ir.pushkareva@gmail.com
DOI: http://dx.doi.org/10.2355/isijinternational.53.1215

for the prediction of stretch-flange formability have recently been developed[15–20] and the appropriate fracture criteria have been assessed.[21] In all these studies, the martensite phase was treated as a homogeneous inclusion in a softer ferrite matrix. This is clearly a simplification which needs to be validated. In this work, we examine in detail the evolution of the martensite phase fraction and carbon distribution using laboratory cold-rolled dual-phase steels prepared from the same industrial hot band, as a function of annealing and tempering conditions.

2. Experimental Procedure

Direct quenching heat treatments were applied to a cold rolled full hard Fe–0.15C–0.215Si–1.9Mn–0.195Cr wt.% industrial strip of thickness 1.2 mm in order to obtain different dual phase microstructures (**Fig. 1**). To be representative of industrial conditions, the samples were heated at 2.7°C/s to six different intercritical annealing temperatures between Ac1 (746°C) and Ac3 (845°C), held at temperature for 130 s and then water quenched to 20°C. For tempering studies, specimens were post-heated at 230°C, 380°C and 460°C for 240 seconds. These temper treatments are compatible with the capacities of overageing sections on current industrial continuous annealing lines. The annealing and quenching experiments were carried out in a continuous annealing simulator whereas the tempering treatments were performed in a salt bath. The microstructures were observed by optical microscopy after Nital and Picral etching and the phase fractions were determined by an Aphelion® semi-automatic image analyzer. More detailed microstructural observations were carried out in a LEO 982 FEG-SEM. SEM samples were mechanically polished to 1 μm using diamond paste and then etched with 2% Nital or Picral and Metabisulfite. Transmission electron microscopy (TEM) observations were carried out in a Philips CM200 FEG-TEM on thin foils prepared in the plane of the sheet at ¼ thickness. The samples were mechanically polished to 50 μm, then pre-thinned to 20 μm by dimpling and finally reduced to electron transparency by twin-jet electropolishing using a solution consisting of 5% perchloric acid in acetic acid at a temperature of 15°C. Local carbon concentration measurements were made on the same foils using a Gatan 666 Electron Energy Loss (EELS) spectrometer employing a specifically developed measurement technique with a detection limit for carbon in an iron matrix of 0.04 wt.%. and a relative error (in the range of C concentrations between 0.2 wt.%. and 0.8 wt.%.) of ± 5%.[22] The EELS experiments were carried out at a temperature of –169°C in a liquid nitrogen cooling holder in order to eliminate carbon contamination on the specimen surface during analysis. Quantitative carbon and manganese segregation maps at medium spatial resolution (~1 μm) were obtained using a Cameca SX50 Electron Probe Microanalyser (EPMA). In addition, high spatial resolution secondary ion mass spectrometry (SIMS) images showing qualitative carbon distribution maps were generated using a Cameca NanoSIMS 50 instrument. The latter was operated with a Cs^+ primary ion beam and has a detection limit for carbon in iron below 0.006 wt.%. and a limiting spatial resolution of 50 nm.[23] High spatial resolution SIMS carbon maps were acquired on samples quenched from 755°C, 790°C and 810°C. The incident Cs^+ probe energy was 16 keV with a primary ion beam current of 1 pA and a probe size between 50 nm and 150 nm. The chamber pressure was 3×10^{-10} Torr and samples were pre-sputtered to eliminate carbon surface contamination. Note that although the SIMS intensity varies linearly with carbon concentration,[23] the data presented here are not quantitative because any reference sample corresponding to the studied grade was used for calibration. Nevertheless, on each carbon map, the variations of C intensity can be interpreted as relative variations in the local C concentration. Moreover, the sensitivity of the technique is enough high to highlight small variation of C concentration as already demonstrated in ferrite.[24] Flat tensile samples of 50 mm gauge length and 12.5 mm width were tested following the European standard EN 10002-1 with the tensile loading axis parallel to the transverse direction of the sheet. The testing speed was 0.008 s^{-1}. The reduction of area (RA) values at fracture were determined using optical microscopy. Hole Expansion (HE) tests were carried out according to the ISO TC 164 specifications. A hole with diameter D_0=10 mm was mechanically punched in the central part of a (100 × 100 mm) test piece. The hole was then expanded burr upwards by a conical punch with a top angle of 60°. The test was stopped when the first visible crack traversed the full thickness of the test piece. The hole expansion ratio HE was then determined by the following formula:

$$HE = \frac{D_h - D_0}{D_0}.$$

where D_0 is the initial hole diameter, and D_h is the hole diameter at fracture.

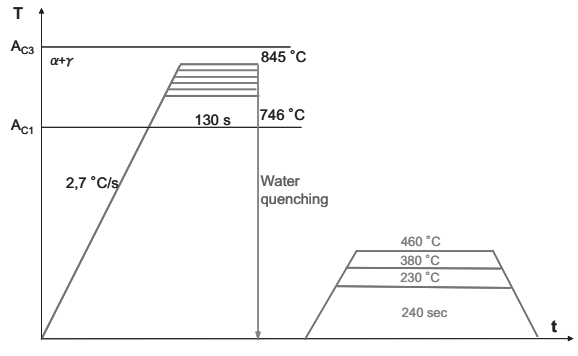

Fig. 1. Schematic showing thermal processing simulations.

3. Results

3.1. Microstructural Characterisation

3.1.1. As-quenched Condition

The microstructures of the as-quenched samples consist of a mixture of martensite and ferrite (**Fig. 2**). The martensite phase is continuous around the ferrite islands. In samples annealed at 810°C and above the ferrite volume fraction is low (less than 1%) and the microstructure is almost fully martensitic (no residual austenite was detected). For each annealing temperature, **Table 1** shows the average ferrite grain size measured in the plane defined by the rolling direction (RD) and the sheet normal (ND), as well as the average thickness of the martensite bands measured in the same

Table 1. Average grain size of ferrite and martensite phases measured in the RD×ND plane for different annealing temperatures.

Annealing temperature, °C	Average ferrite grain size, μm	Average thickness of martensite bands, μm
755	5.6	2.5
763	6.1	2.6
785	4.1	4.1
790	5.6	4.2
810	3.1	–
840	1.3	–

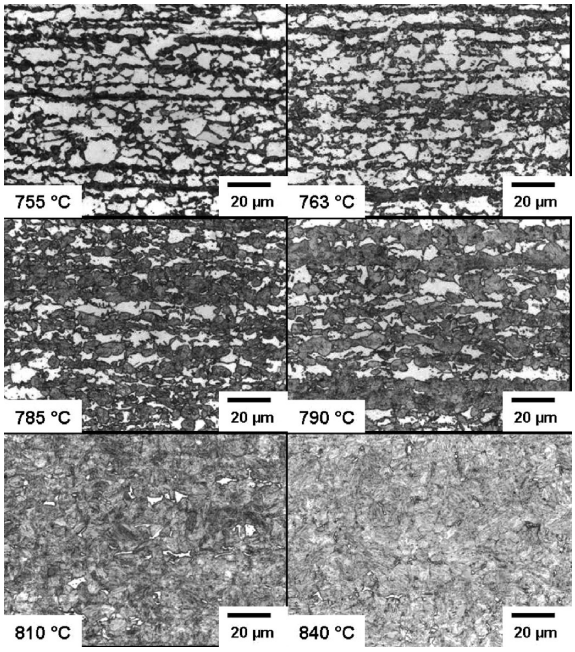

Fig. 2. Optical micrographs of the as-quenched samples. Picral and Metabisulfite etching: the dark-etching phase is martensite, the white-etching phase is ferrite.

plane in the normal direction.

EPMA carbon and manganese maps (**Fig. 3**) at ½ thickness from a sample quenched at T_Q = 760°C confirmed that the banded martensite structure is related to co-segregated Mn and C.[25] The Mn concentration varied from 1.5 wt.%. to 3.2 wt.%. for a nominal of 1.9 wt.%. and the average C concentration in the martensite was measured to be 0.24% wt. **Figure 4**(a) shows the variation of the experimental martensite fraction with quenching temperature as determined by image analysis. These data should be compared with values obtained by equilibrium thermodynamic modelling using the Ceqsci® software.[26] It can be seen that the experimental martensite fraction is slightly higher than that given by the model predictions. This will be discussed further later on.

Further evidence that the system achieves at least partial thermodynamic equilibrium during intercritical holding can be taken from the EELS martensite carbon concentrations shown on Fig. 4(b). The EELS measurements were averaged over at least 5 different martensite islands or colonies in each foil and the electron probe was defocused so that the mean carbon content in the island was probed, taking care not to include any ferrite in the analysed volume. Comparing the data with the equilibrium values calculated in Fig. 4(b), it can be seen that there is an excellent agreement between experiment and model. It is also satisfying to note that the EELS C content for samples quenched at 760°C was 0.28±0.04% wt., which is comparable with the EPMA data from the same sample.

It is known that the ferrite to austenite transformation is controlled by kinetic effects and that these are likely to be important given the short intercritical annealing time (130 s). However, the above results indicate that the operating tie-line for the transformation must be close to that predicted by equilibrium, for all the tested annealing temperatures. Here, we do not speak of thermodynamic equilibrium in the true sense because the manganese is certainly not completely partitioned in such a short time.

SIMS C maps from two samples quenched at T_Q = 790°C and 755°C can be seen in **Fig. 5**, along with representative SEM images from the same samples. The carbon content increases from below the detection limit (black) to a maximum (red) in these images. Several interesting points can be made. Firstly the C concentration in the as-quenched martensite is heterogeneous at all annealing temperatures (including 810°C)[1]. As expected, the average C content in the martensite quenched from 755°C is higher than that formed from 790°C. At T_Q = 790°C, a clear enrichment in the C content occurs at ferrite/martensite interfaces, whereas at T_Q = 755°C it appears that the opposite is true and that C is depleted near the phase boundaries. Carbon enrichment was also seen at T_Q = 810°C. From the higher magnification images the C-enriched regions in the 790°C sample extend over a distance of typically 0.8 μm whereas the C-depletion region at 755°C appears to be narrower, around 0.3 μm in width.

High resolution EELS data were acquired from the interface to the centre of a ~3 μm diameter martensite island in the 755°C as-quenched sample to try to quantify the change in the interface C concentration. The results can be seen in **Fig. 6**. Here the probe radius was 0.1 μm so some overlapping of the analysed volume occurs near the phase boundary. It was checked that the martensite island extended through the thickness of the foil.

The EELS line scan confirms that the C concentration is heterogeneous inside the martensite with a minimum of 0.19±0.01% wt. C at the interface and a maximum of 0.26±0.013% wt. C occurring at a distance of 0.3 μm from the ferrite. This behaviour is consistent with the qualitative C maps from the SIMS nanoanalysis in Fig. 5.

3.1.2. As-tempered Condition

During tempering, martensite decomposition will eventually tend to form a ferrite/cementite structure.[27] After tempering at a temperature T_T = 230°C for 240 s, carbide precipitates are observed in the martensite (**Fig. 7**(a)). The precipitation is more pronounced at higher tempering temperatures (Figs. 7(b) and 7(c)). Coarsening of these carbide precipitates occurs during 460°C tempering. Carbide chains can also be

[1]Note that it was checked by TEM that no auto-tempered carbides were detectable in any of these samples.

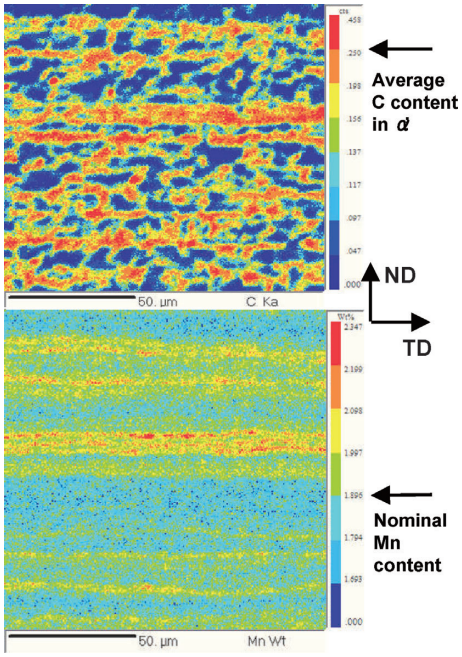

Fig. 3. EPMA carbon (a) and manganese (b) maps of a sample quenched from 760°C (plane ND (normal direction) × TD (transverse direction) imaged at 1/2 thickness).

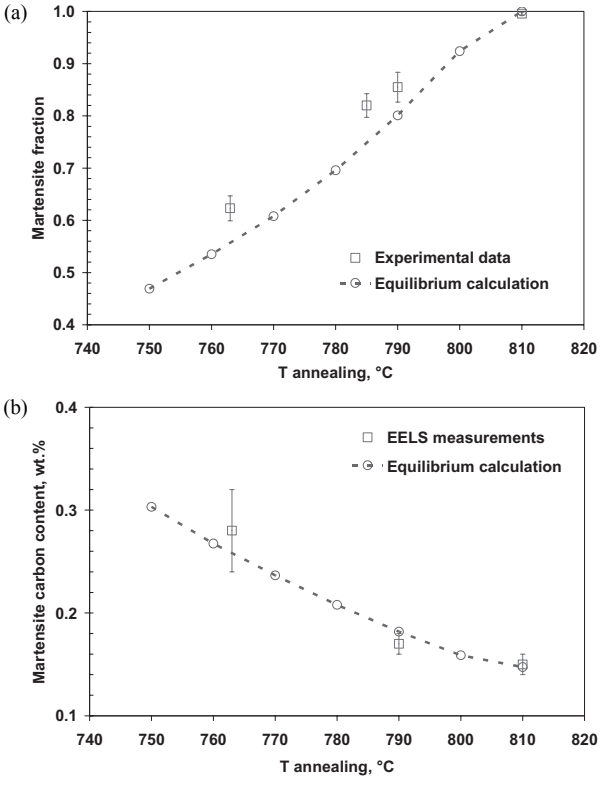

Fig. 4. (a) A comparison of the experimentally measured martensite fraction for different annealing temperatures with values calculated assuming equilibrium conditions. (b) A comparison of the experimentally measured carbon concentrations in martensite by EELS with values calculated under equilibrium conditions and from a mass balance.

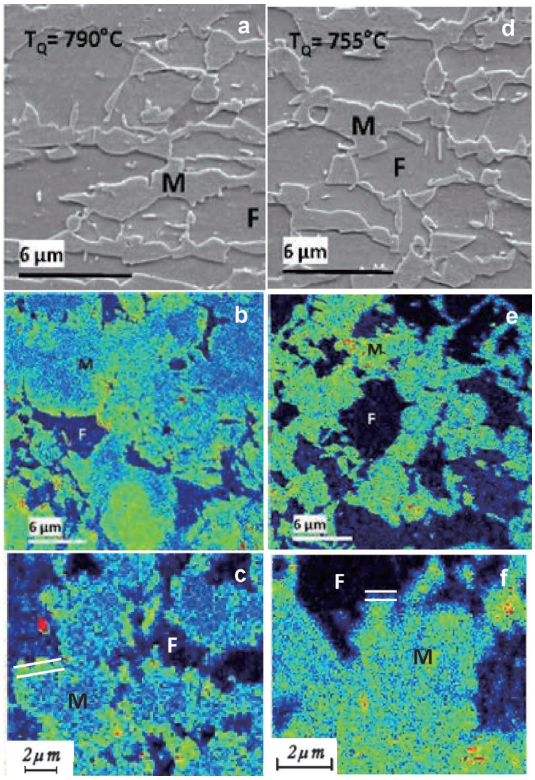

Fig. 5. SEM Images (a, d) and qualitative SIMS carbon maps (b, c, e, f) from samples direct quenched from 790°C (a–c) and 755°C (d–f). The carbon content increases from black to red. Carbon enriched and depleted zones are indicated by parallel lines. M stands for martensite and F for ferrite.

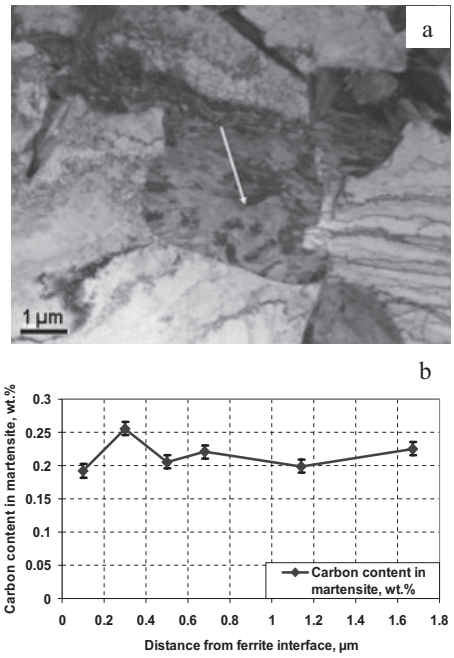

Fig. 6. TEM image of a martensite island in as-quenched T_Q = 755°C sample (a) and (b) EELS C concentration measurements taken from the ferrite interface to the centre of the island following the arrow.

seen at martensite/ferrite boundaries in the ferrite-martensite microstructure (Fig. 7(b)) and at martensite/martensite (prior austenite) grain boundaries in fully martensitic microstructures (Fig. 7(c)). Further, carbide chains are observed inside the martensite, at lath boundaries. This is in accordance with the observations of Speich,[28] where the larger particles lying on interlath boundaries grow at the expense of the intra-lath particles, resulting in a final dispersion of

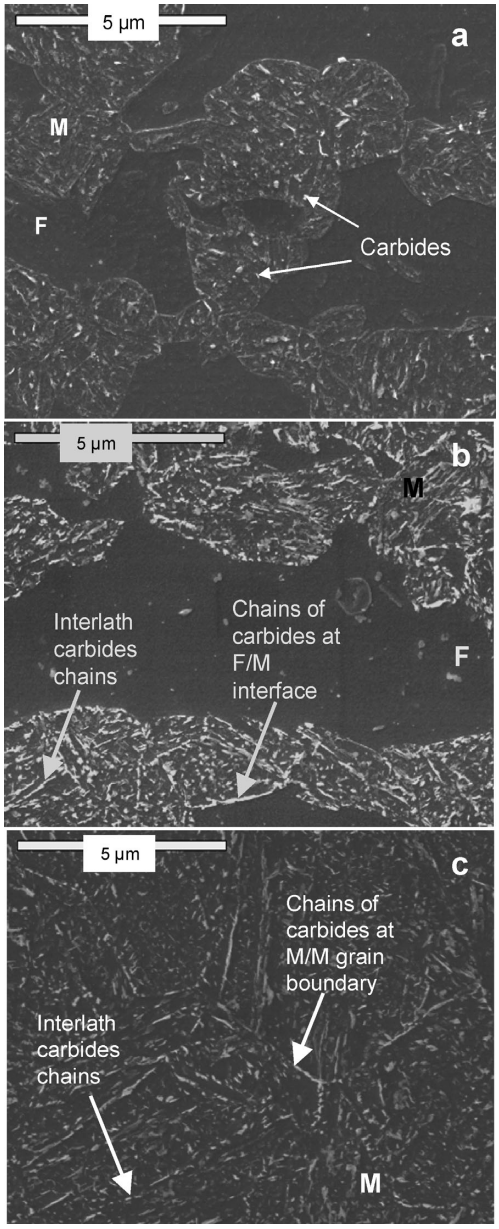

Fig. 7. SEM micrographs showing the evolution of different microstructures with tempering. Picral etching. a) T_Q = 755°C, T_T = 230°C, b) T_Q = 755°C, T_T = 460°C, c) T_Q = 810°C, T_T = 460°C.

cementite particles only on interlath boundaries.

The ionic carbon maps in **Fig. 8** show the effect of increasing the tempering temperature on the C distribution in the martensite of the samples quenched at T_Q = 755°C and T_Q = 810°C. In both cases, carbide precipitates can be detected inside the martensite islands after tempering for 240 s at T_T = 230°C, however this is most evident in the specimen quenched from 755°C, probably due to the higher initial martensite C concentration. At T_T = 460°C the carbide precipitation is more pronounced, and C-depleted regions appear in the martensite next to these particles. For the 755°C sample, very few precipitates are found at the ferrite interface, suggesting that the C-depleted zone in the as-quenched sample retards carbide formation. Figure 8 also shows that the tempering behaviour of the sample quenched from 810°C is quite different. The carbide distribution appears to be more dense and finer at T_T = 230°C. This effect is especially clear at T_T = 460°C where carbides strongly decorate the ferrite/martensite boundaries. Thus it appears that the C enrichment at the ferrite/martensite interface shown in Figs. 5 and 6 leads to faster carbide precipitation at the phase boundary. Samples tempered at T_T = 380°C showed exactly the same trends, with an intermediate behaviour.

4. Discussion

4.1. Understanding the Carbon Distribution

We assume that the carbon distribution in the as-quenched martensite is completely determined by the carbon profile generated in the austenite at the end of the isothermal hold *i.e.* no significant carbon redistribution occurs during or after quenching to room temperature. It is known that the nucleation of austenite in ferrite-pearlite structures occurs first at carbides.[29] Once austenite has nucleated in pearlite, its subsequent growth is presumably controlled by the rate of carbon diffusion in the austenite.[30] In our case, austenite nucleates first on cementite particles formed in the hot band during coiling. This cementite has a Mn concentration higher than that of the ferrite matrix for several reasons:[31]

1. Carbides tend to form in Mn segregated zones,
2. Carbides are enriched in Mn during the formation process.

The austenite formation stages are as follows:

- cementite dissolution stage,
- austenite growth.

Figure 9 shows an austenite formation diagram,[29] which indicates the controlling kinetic processes. Using this diagram, the steps in austenite formation can be identified for a given annealing temperature and time.

According to this diagram, during intercritical annealing austenite growth is controlled initially by cementite dissolution, then the rapid carbon diffusion in austenite and subsequently by Mn diffusion in ferrite and in the growing austenite. The latter step is rate limiting, due to the slow diffusion of Mn in austenite.

In **Fig. 10**(a) and 10(b) we plot the expected evolution of the tie-lines and the carbon profile during austenite growth at 755°C. The tie-line calculations were done with the THERMOCALC software whereas the carbon profiles are indicative sketches.

Cementite particles provide preferential nucleation sites for austenite. At the beginning of the cementite dissolution process, the austenite forming inherits a sharp manganese profile due to the initial manganese enrichment of cementite. However, when the cementite dissolution is completed, austenite grows at the expense of ferrite. In that case, both C and Mn composition at the α/γ interface depend on thermodynamic and kinetic conditions. It can be shown,[32] that the initial operative tie-line for austenite growth can be determined by a simple argument that the growing phase (austenite) inherits the Mn composition of the ferrite at the α/γ interface. This determines the operative tie-line at t_1 (see Fig. 10(a)).

As the transformation progresses the operative tie-line moves in the phase diagram and the speed of this displacement depends on the annealing temperature. At 755°C the C concentration at the α/γ interface (on the austenite side)

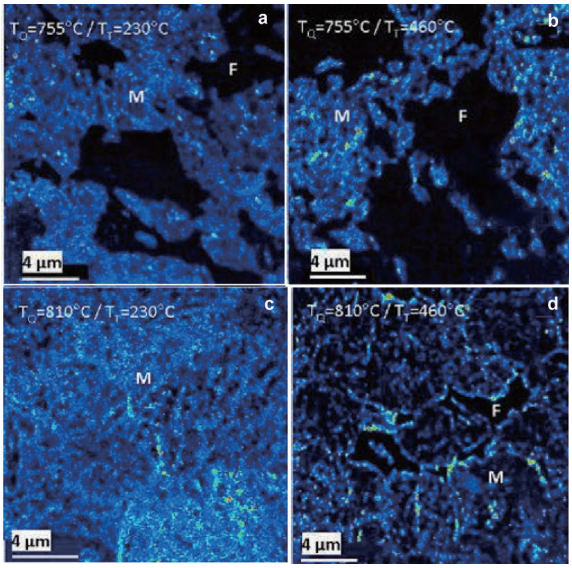

Fig. 8. Qualitative SIMS carbon maps from samples quenched at T_Q = 755°C (a, b) and T_Q = 810°C (c, d) and tempered at 230°C (a, c) and 460°C (b, d). The carbon content increases from black to red.

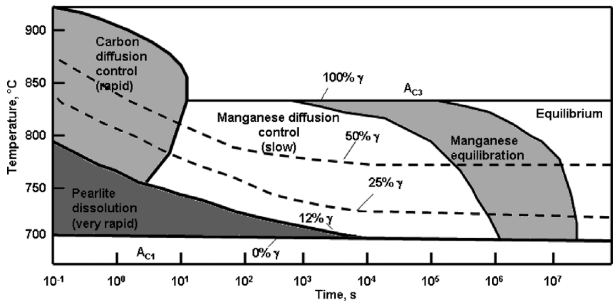

Fig. 9. Austenite growth diagram for Fe–0.12C–1.5Mn–0.24Si steel.[29]

will decrease and the Mn concentration will increase as the austenite fraction increases (Fig. 10(b)). The carbon profile shapes show a clear C depletion in austenite near the interface, compared with the value far from the interface. It is interesting to note that the tie-line at t_3 can be higher than the equilibrium tie-line t_2. This is one possible explanation for the fact that the measured martensite fraction in Fig. 4(a) is systematically higher than the equilibrium prediction. Under these conditions it is reasonable to suppose that the austenite growth is controlled by C and Mn diffusion in austenite.

At higher transformation temperatures (790°C) the initial operating tie-line t_1 is very close to that given by equilibrium (see the red circle in **Fig. 11**(a)). The area swept out by the movement of the operative tie-line at 790°C will therefore be more restricted than at 755°C. Moreover, the Mn diffusion coefficient in austenite is higher at 790°C so that we might expect to observe a different transformation behaviour at the higher temperature, and this is confirmed by our results.

From Fig. 11(b) the C concentration on the austenite side of the interface decreases between t_1 and t_2 as before. The austenite is growing and, unlike the low temperature case, the operating tie-line t_2 is above that predicted at equilibrium. During this stage, Mn will tend to accumulate at the

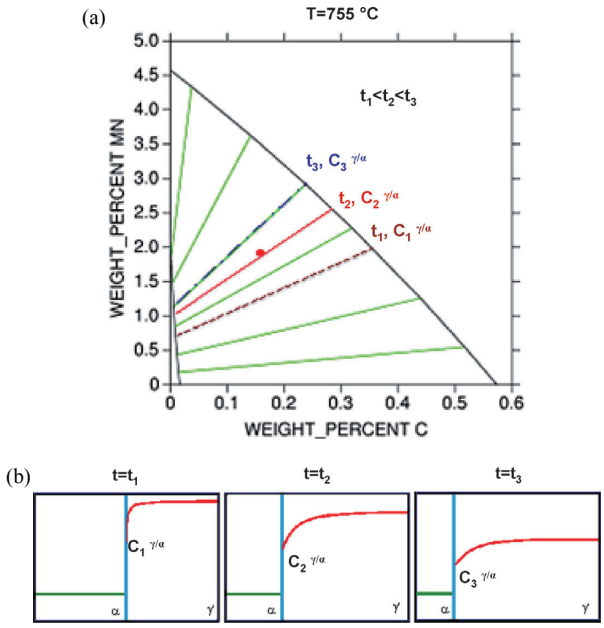

Fig. 10. (a) Expected evolution of the tie-lines during austenite growth at 755°C for Fe–0.15C–0.215Si–1.9Mn–0.195Cr. The calculations were done with the THERMOCALC software. The red circle indicates the nominal composition and the equilibrium tie-line is the solid red line marked t_2. (b) Schematic showing the expected evolution of the carbon profiles during austenite growth at 755°C for Fe–0.15C–0.215Si–1.9Mn–0.195Cr.

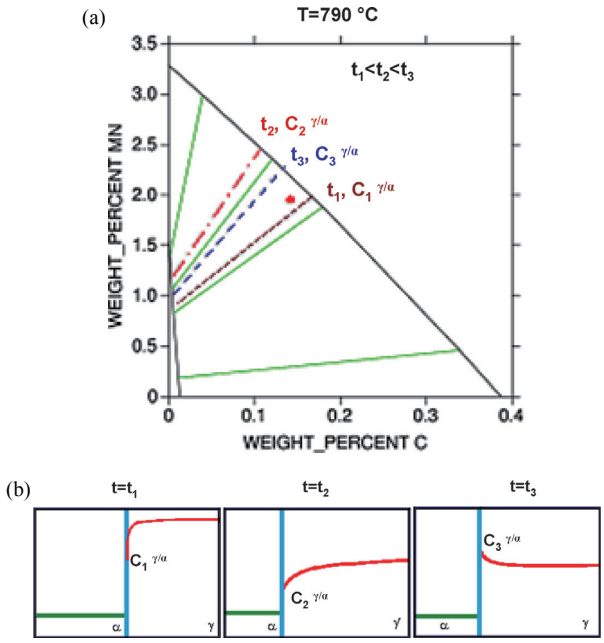

Fig. 11. (a) Expected evolution of the tie-lines during austenite growth at 790°C for Fe–0.15C–0.215Si–1.9Mn–0.195Cr. The calculations were done with the THERMOCALC software. The red circle indicates the nominal composition and the equilibrium tie-line is the solid red line marked t_2. (b) Schematic showing the expected evolution of the carbon profiles during austenite growth at 790°C for Fe–0.15C–0.215Si–1.9Mn–0.195Cr.

austenite side of the interface. This Mn must be redistributed inside the austenite to homogenize the concentration. However, at this point the Mn composition in austenite at the interface is higher than that predicted by thermodynamic

equilibrium. A Mn flux will therefore be created which will allow the ferrite to grow at the expense of austenite. This is a mean for the system to equilibrate Mn. From t_2 to t_3 the carbon concentration will therefore increase at the austenite side of the α/γ interface (Fig. 11(b)).

It is usually believed that this process only occurs after extended isothermal holding of the order of 10^4 s at 790°C as the Mn diffusion coefficient is very low in austenite.[1] However, some recent experimental results exist which show that Mn can start to partition in austenite even at short times (10^2 s).[33] There are two possible explanations: the Mn could diffuse rapidly along grain boundaries or an initial heterogeneous Mn distribution could influence the tie-line movement.[34] The latter could take its origin in micro-segregation bands inherited from the solidification process, or from the dissolution of Mn enriched cementite.

4.2. Implications for in-use Properties

The microstructure/properties relations for as-quenched DP steels proposed by Delincé *et al.*[3] clearly illustrate that there are multiple possible compositions and processing routes to attain any target set of tensile parameters (YS, UTS, El). If we then take into account additional adjustable process parameters such as tempering temperature and time then the number of potential solutions increases even further. In practice, designing a target DP grade based on say, tensile properties and weldability is rather easy and there are many commercial products available. However, the main weakness of DP steels lies in their limited stretch flange formability and resistance to damage. It is by controlling the latter properties that the most successful products are distinguished. Most studies of ductile damage mechanisms in DP steels highlight the important contribution of the formation of voids by decohesion at ferrite/martensite interfaces, followed by the propagation of microfissures at the phase boundaries.[4,5,7,10] It seems reasonable then to question whether or not the presence of a strong carbon gradient at the ferrite/martensite interface could significantly modify this process.

Often the cohesive strength of the ferrite/martensite interface is modelled using an energy criterion necessary for the creation of new surfaces and either a stress or a local strain criterion for debonding. The Argon criterion describes such a critical stress σ_c for hard inclusions larger than ~20 nm.[35] This stress state is the sum of the hydrostatic stress σ_h and the Von Mises equivalent stress σ_{eq}:

$$\sigma_c = \sigma_{eq} + \sigma_h \quad \text{..... (1)}$$

This can be related to the macroscopic stress triaxiality T which is just the ratio σ_h/σ_{eq} so that:

$$\sigma_c = \sigma_{eq}(1+T) \quad \text{..... (2)}$$

The local value of T at the ferrite/martensite interface may be higher than the macroscopic value due to the kinematic hardening X generated by strain incompatibilities between the two phases.[36] Equation (2) is thus modified:

$$\sigma_c = \sigma_{eq}\left(1+T\left(\frac{\sigma_{eq}}{\sigma_{eq}-X}\right)\right) \quad \text{..... (3)}$$

If the macroscopic strain just at the start of void nucleation ε_n in a tensile test is measured then the stress acting on the interface is:

$$\Sigma_{\varepsilon_n} = \sigma_{eq}\left(1+T\left(\frac{\sigma_{eq}}{\sigma_{eq}-X_{\varepsilon_n}}\right)\right) \quad \text{..... (4)}$$

T can be determined (for example using the Bridgman formula[37]) and σ_{eq} can be calculated by measuring the sample section at $\varepsilon = \varepsilon_n$. The value of the backstress X_{ε_n} can be estimated from the relation:[38]

$$X_{\varepsilon_n} = (1-f_m) f_m \Delta\sigma_{\varepsilon_n} \quad \text{..... (5)}$$

where f_m is the martensite volume fraction and $\Delta\sigma_{\varepsilon_n}$ is the difference in the flow stress of the two phases at the nucleation strain. An approximate value for $\Delta\sigma_{\varepsilon_n}$ can be calculated by noting that the macroscopic void nucleation strains ε_n in DP steels are generally quite high ($\varepsilon_n > 0.2$)[39] so that strain hardening can be assumed to be saturated. Thus it is probably not unreasonable to replace $\Delta\sigma_{\varepsilon_n}$ by the difference in the *UTS* values of the constituent phases. For ferrite this is essentially determined by the initial grain size, whereas for martensite it is the carbon concentration which is the critical parameter. A useful empirical expression for the latter, developed by Buessler[40] is:

$$UTS = 3\left(\alpha - \left(\frac{1}{\beta+\gamma[\%C]}\right)^{\delta}\right) \quad \text{..... (6)}$$

where $\alpha = 950.44$, $\beta = 0.9688$, $\gamma = 0.01274$, $\delta = 208.676$ and C is in wt.%. Using Eq. (6) the martensite flow stress at the ferrite interface of the martensite island shown in Fig. 6 is ~1 522 MPa (0.19 wt.%. C), *i.e.* 16% lower than the mean value of ~1 812 MPa (corresponding to the macroscopic average martensite carbon concentration of 0.28 wt.%.). Of course, this does not mean that the backstress X_{ε_n} at the interface will be reduced in the same proportion, but it does place an upper limit on the effect.

For a microstructure with f_m = 0.5 and assuming a *UTS* value for ferrite of 450 MPa, the upper limit for the decrease in X_{ε_n} using Eq. (5) would be ~20% (from 340 MPa to 268 MPa). We can estimate the effect that this would have on Σ_{ε_n} by assuming T = 0.3 (for a plane tensile specimen before necking) and σ_{eq} = 1 000 MPa. When these values are substituted in Eq. (4), Σ_{ε_n} decreases by 3%. A parametric study where the martensite fraction f_m was varied between 0.3 and 0.6, T was varied between 0.3 and 0.6 and σ_{eq} between 700 MPa and 1 000 MPa showed that the maximum decrease in Σ_{ε_n} was ~8%.

There are two possibilities:

1. The critical debonding stress σ_c for the ferrite/martensite interface is a material constant independent of the martensite carbon content. In this case the simple analysis above indicates that carbon depletion could induce a beneficial increase in the void nucleation strain ε_n due to a reduction in the backstress at the interface which decreases the local stress triaxiality. Hence the onset of damage should be slightly retarded.

2. The critical debonding stress σ_c varies with the martensite carbon content. A recent literature study by C.Landron[10] comparing the published values of ε_n measured for different DP steels suggests that this is indeed the

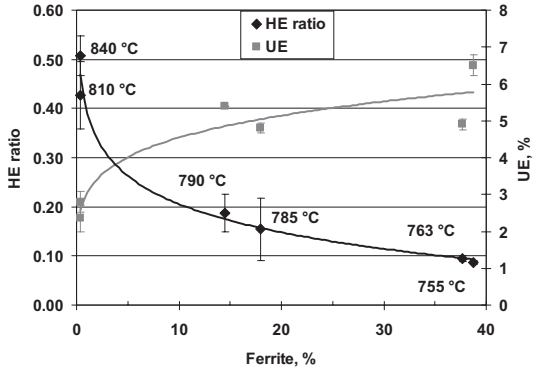

Fig. 12. HE ratio and UE versus ferrite fraction for as-quenched samples. Quenching temperatures are shown in the figure.

case. However, for martensite carbon contents < 0.5 wt.% (which is usually the case for ultra high strength DP steels) σ_c was found to be essentially constant, with a value of 1 200 MPa. Note that this value is significantly lower than the 1.8 GPa – 2.5 GPa obtained by Poruks for a low carbon bainite-martensite steel.[39)]

Hole expansion tests on as-quenched samples revealed a non-intuitive result – the damage resistance increases strongly as the ferrite content decreases, whilst the ductility (as measured by the uniform elongation in tensile tests) showed the opposite trend (**Fig. 12**). The variations are so marked that the rather moderate potential improvement in the as-quenched damage resistance discussed above would be very difficult to demonstrate by experiment; maintaining a constant ferrite/martensite ratio while quenching from high and low intercritical temperatures could only be achieved by varying the initial composition, and even small differences in the final ferrite content would have a much bigger effect than that expected from the interfacial carbon depletion.

In specimens quenched from high intercritical temperatures the carbon concentration is enhanced at the ferrite/martensite interface. No quantitative measurements of the amount of carbon enrichment were made in this study so we cannot make any sensible calculations of the likely mechanical consequences. Following the previous argument, we would expect that local carbon enrichment would tend to accelerate the onset of void formation at the interface. However, during tempering, carbide formation is accelerated in these carbon enriched areas so that the ferrite/martensite boundaries are transformed to a more complex ferrite/carbide/tempered martensite structure. At tempering temperatures above 280°C the carbide formed will be cementite. The critical debonding stress σ_c for the ferrite/cementite interface has been studied by several authors. For example, Kwon[41)] and Le Roy[42)] independently determined σ_c =1 200 MPa for this interface and there appears to be some consensus around this figure. It is often claimed that the ferrite/martensite interface has a higher critical debonding stress than that of ferrite/cementite,[7] based on the high σ_c values published by Poruks.[39)] However, the difference may not be so great if the calculations of Landron[10)] are taken into account.

The influence of tempering on the HE and RA parameters as a function of intercritical annealing temperature can be seen in **Figs. 13**(a) and 13(b). Clearly there is a strong beneficial effect which increases as the tempering temperature is raised. It is interesting to note that the gain in damage resistance (HE/RA) as a function of tempering temperature is greatest for specimens quenched from the lower temperatures (760°C) *i.e.* those with carbon depleted ferrite/martensite interfaces. This is especially evident in the RA data, where measurement errors are smaller. We have shown elsewhere[43)] that one of the major effects introduced by tempering in DP steels is to change the damage mode; in as-quenched samples the main damage mechanism is either decohesion at ferrite/martensite interfaces or internal cavity formation in martensite (depending on the amount of martensite formed) whereas after tempering voids form preferentially at carbide/martensite interfaces. Tomographic X-ray analysis showed that the rate of void formation as a function of strain during tensile testing was reduced by a factor of ~4 after tempering. Furthermore, these carbide/martensite cavities were distributed more uniformly in the microstructure and their density at final fracture was higher, suggesting that void growth is slower after tempering. Given this mechanism it is reasonable to infer that the improvement in damage resistance due to dispersed void formation at tempered carbides will be compromised if those carbides are localised at ferrite/martensite interfaces (Fig. 8). This argument mitigates for the carbon-depleted interface structure obtained at lower intercritical temperatures.

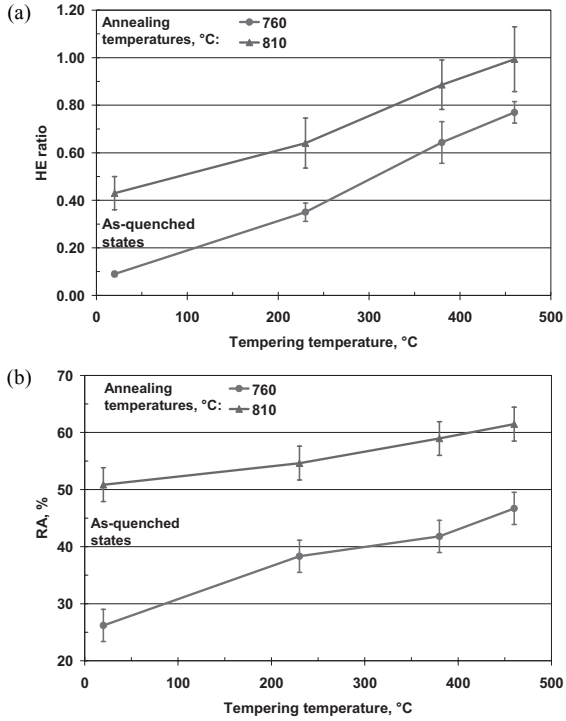

Fig. 13. (a) HE ratio evolution with tempering temperature for 760°C and 810°C annealing temperatures. (b) Variation in the reduction of area (RA) with tempering temperature for 760°C and 810°C annealing temperatures.

5. Conclusions

We have carried out a systematic and detailed study of the microstructural evolution of martensite in as-quenched and quenched and tempered ultra high strength Fe–0.15C–0.215Si–1.9Mn–0.195Cr dual phase steels processed to give

four different ferrite/martensite ratios. A comparison of the experimental martensite phase fractions and average carbon concentration with thermodynamics modeling predictions showed that partial thermodynamic equilibrium was obtained after intercritical annealing for 130 s. However, it was found that the local carbon distribution in as-quenched martensite was heterogeneous for all quenching temperatures. Significant carbon enrichment was observed at the ferrite/martensite interface at annealing temperature of 790°C, whereas carbon depletion occurred when the annealing temperature was reduced to 755°C. A possible explanation for the carbon profile in terms of the effect of Mn partitioning on the austenite phase transformation kinetics is given. During subsequent tempering, the carbon gradient at the interface strongly modifies the precipitation kinetics of carbides; DP steels quenched from high temperatures showed fast precipitation of carbides at ferrite/martensite interfaces during tempering in the range 230–460°C. On the other hand, alloys with carbon-depleted interfaces had a much more homogeneous carbide distribution. Thus the nature of the ferrite/martensite interface is very sensitive to the processing conditions. A simple analysis was applied to estimate the maximum impact of the heterogeneous carbon profile in martensite on damage behaviour in as-quenched samples. If we assume that the critical debonding stress σ_c for the ferrite/martensite interface is a material constant (*i.e.* independent of the martensite carbon content) then the interface carbon depletion observed at lower intercritical annealing temperatures could induce a beneficial increase in the void nucleation strain ε_n. This effect is due to a reduction in the backstress at the ferrite/martensite interface which decreases the local stress triaxiality. We estimate that the upper limit for the improvement is ~8%, so the effect could provide a moderate delay in the onset of damage. Further, we propose that the improvement in damage resistance due to tempering is mainly due to dispersed void formation at tempered carbides and that this mechanism will be compromised if those carbides are localised at ferrite/martensite interfaces. Experimental HE and RA data appears to be consistent with this hypothesis. This argument mitigates for the carbon-depleted interface structure obtained at lower intercritical temperatures.

REFERENCES

1) G. R. Speich: Proc. Int. Conf. Fundamentals of Dual-phase Steels, Metallurgical Society of AIME, Warrendale, PA, (1981), 3.
2) B. K. Zuidema: *JOM*, **64** (2012), No. 9, 1039.
3) M. Delincé, Y. Bréchet, J. D. Embury, M. G. D. Geers, P. J. Jacques and T. Pardoen: *Acta Mater.*, **55** (2007), 2337.
4) K. Hasegawa, K. Kawamura, T. Urabe and Y. Hosoya: *ISIJ Int.*, **44** (2004), No. 3, 603.
5) A. Cingara, Y. Ososkov, M. K. Jain and D. S. Wilkinson: *Mater. Sci. Eng.* A, **516** (2009), 7.
6) T. Ishiguro, Y. Yoshida, N. Yukawa, T. Ishikawa, H. Yoshida and N. Fujita: *Tetsu-to-Hagané*, **97** (2011), No. 3, 38.
7) J. Kadkhodapour, A. Butz and S. Ziaei Rad: *Acta Mater.*, **59** (2011), 2575.
8) E. Maire, O. Bouaziz, M. Di Michiel and C. Verdu: *Acta Mater.*, **56** (2008), 4954.
9) C. Landron, O. Bouaziz, E. Maire and J. Adrien: *Scr. Mater.*, **63** (2010), 973.
10) C. Landron, E. Maire, O. Bouaziz, J. Adrien, L. Lecarme and A. Bareggi: *Acta Mater.*, **59** (2011), 7564.
11) J. Kang, Y. Ososkov, J. D. Embury and D. S. Wilkinson: *Scr. Mater.*, **56** (2007), 999.
12) A. M. Sarosiek, M. Grujicic and W. S. Owen: *Scr. Metall.*, **18** (1984), 353.
13) Y. Tomota, M. Umemoto, N. Komatsubara, A. Hiramatsu, N. Nakajima, A. Moriya, T. Watanabe, S. Nanba, G. Anan, K. Kunishige, Y. Higo and M. Miyahara: *ISIJ Int.*, **32** (1992), No. 3, 343.
14) Z. Jiang, Z. Guan and J. Lian: *Mat. Sci. Eng. A*, **190** (1995), 55.
15) M. S. Niazi, H. H. Wisselink, T. Meinders and J. Huétink: *Int. J. Damage Mech.*, **21** (2012), 713.
16) M. G. Lee, J. H. Kim, D. K. Matlock and R. H. Wagoner: Proc. 10th Int. Conf. NUMIFORM, eds. by F. Barlat, Y. H. Moon and M. G. Lee, American Institute of Physics, New York, (2010), 149.
17) O. West, J. Lian, S. Munstermann and W. Bleck: *ISIJ Int.*, **52** (2012), No. 4, 743.
18) N. Vajragupta, V. Uthaisangsuk, B. Schmaling, S. Munstermann, A. Hartmaier and W. Bleck: *Comp. Mater. Sci.*, **54** (2012), 271.
19) V. Uthaisangsuk, U. Prahl and W. Bleck: *Comp. Mater. Sci.*, **45** (2009), 617.
20) S. K. Paul: *Comp. Mater. Sci.*, **56** (2012), 4.
21) G. Gruben, O. S. Hopperstad and T. Borvik: *Int. J. Mech. Sci.*, **62**, (2012), No. 1, 133.
22) C. P. Scott and J. Drillet: *Scr. Mater.*, **56** (2007), 89.
23) N. Valle, J. Drillet, O. Bouaziz and H-N. Migeon: *Appl. Surf. Sci.*, **252** (2006), 7051.
24) N. Valle, J. Drillet, A. Perlade and H-N. Migeon: *Appl. Surf. Sci.*, **255** (2008), 1569.
25) B. Krebs, L. Germain, A. Hazotte and M. Goune: *J. Mater. Sci.*, **46** (2011), 7026.
26) J. Lehmann: *Rev. Métall.*, **1** (2008), 539.
27) G. R. Speich, A. J. Schwoeble and G. P. Huffman: *Metall. Trans. A*, **14** (1983), 1079.
28) G. R. Speich and K. A. Taylor: Martensite, ASM International, OH, (1992).
29) G. R. Speich, V. A. Demarest and R. L. Miller: *Metall. Trans. A*, **12** (1981), 1419.
30) G. R. Speich: *Trans. AIME*, **245** (1969), 2553.
31) M. Gouné, J. Drillet and P. Maugis: Proc. Int. Conf. On Solid State Phase Transformations in Inorganic Materials, TMS, Warrendale, PA, (2005), 843.
32) T. Iung, M. Azuma, O. Bouaziz, M. Gouné, A. Perlade and D. Quidort: *Mater. Sci. Forum.*, **426** (2003), No. 4, 3849.
33) Y. Toji, K. Nakajima, T. Yamashita, K. Okuda, H. Matsuda, K. Hasegawa and Y. Tanaka: *CAMP-ISIJ*, **21** (2008), 486.
34) N. Pussegoda, W. R. Tyson, P. Wycliffe and G. R. Purdy: *Metall. Trans. A*, **15** (1984), 1499.
35) A. S. Argon and J. Im: *Metall. Trans. A*, **6** (1975), 839.
36) A. L. Helbert, X. Feaugas and M. Clavel: *Acta Mater.*, **46** (1998), No. 3, 939.
37) P. W. Bridgman: *Rev. Mod. Phys.*, **17** (1945), 3.
38) S. Allain and O. Bouaziz: *Mater. Sci. Eng.*, **496A** (2008), 329.
39) P. Poruks, I. Yakubtsov and J. D. Boyd: *Scr. Mater.*, **54** (2006), 41.
40) P. Buessler and T. Iung: IRSID Internal Report, MPM 99/2173, IRSID, Maizières-lès-Metz, (1999).
41) D. Kwon: *Scr. Metall.*, **22**, (1988), 1161.
42) G. Le Roy, J. D. Embury, G. Edward and M. F. Ashby: *Acta Metall.*, **29** (1981), 1509.
43) I. Pushkareva: PhD Thesis, University of Lorraine, (2009).